



## Ultrasound artificially nucleated bubbles and their sonochemical radical production

David Fernandez Rivas<sup>a,\*,1</sup>, Laura Stricker<sup>b,1</sup>, Aaldert G. Zijlstra<sup>b</sup>, Han J.G.E. Gardeniers<sup>a</sup>, Detlef Lohse<sup>b</sup>, Andrea Prosperetti<sup>b,c</sup>

<sup>a</sup> Mesoscale Chemical Systems Group, MESA+ Research Institute, University of Twente, P.O. Box 217, 7500 AE Enschede, The Netherlands

<sup>b</sup> Physics of Fluids Group, Department of Applied Physics, Faculty of Science, University of Twente, P.O. Box 217, 7500 AE Enschede, The Netherlands

<sup>c</sup> Department of Mechanical Engineering, Johns Hopkins University, Baltimore, MD 21218, USA

### ARTICLE INFO

#### Article history:

Received 14 March 2012

Received in revised form 21 July 2012

Accepted 26 July 2012

Available online 9 August 2012

#### Keywords:

Radicals  
Sonochemistry  
Ultrasound  
Microfabrication  
Bubbles

### ABSTRACT

We describe the ejection of bubbles from air-filled pits micromachined on a silicon surface when exposed to ultrasound at a frequency of approximately 200 kHz. As the pressure amplitude is increased the bubbles ejected from the micropits tend to be larger and they interact in complex ways. With more than one pit, there is a threshold pressure beyond which the bubbles follow a trajectory parallel to the substrate surface and converge at the center point of the pit array. We have determined the size distribution of bubbles ejected from one, two and three pits, for three different pressure amplitudes and correlated them with sonochemical OH<sup>•</sup> radical production. Experimental evidence of shock wave emission from the bubble clusters, deformed bubble shapes and jetting events that might lead to surface erosion are presented. We describe numerical simulations of sonochemical conversion using the empirical bubble size distributions, and compare the calculated values with experimental results.

© 2012 Elsevier B.V. All rights reserved.

### 1. Introduction

Sonochemistry, the use of ultrasound in chemistry and processing [1], is a very promising field with applications in e.g. nanomaterials synthesis, degradation of contaminants in water treatment and the food industry [2–4]. In a sonochemical reactor each bubble acts as a single reactor in itself [5,6], but the spatial distribution of these bubbles is normally not homogeneous, forming filamentary patterns or clusters [7,8]. Establishing the correlation between the sonochemical yield and the size, location and dynamics of the bubbles in these clusters may provide the knowledge to improve the efficiency of sonochemical reactors.

There is a considerable amount of experimental and theoretical work on single bubbles [9,5,10] but, for practical applications, where the interest normally resides in multibubble systems, it turns out to be very difficult to extract bubble sizes and spatial distributions [11,12]. So far only holographic or laser techniques were successful in providing such information while also valuable information was obtained from bubble dissolution measurement [7,13–19]. No study combining bubble distribution, sonochemical conversion and corresponding numerical simulations has been published.

At the root of this problem lies the fact that cavitation and its inception are extremely complex and very difficult to control. Once

the conditions for cavitation inception exist, many phenomena have an influence on the functioning of the sonochemical reactor: bubble–bubble interaction, coalescence, surfactants or impurities dissolved in the liquid altering the bubble population and liquid properties, recirculation of the liquid inside the reactor, energy losses due to viscous heating, degassing of the liquid, energy conversion losses (e.g., electrical-to-mechanical) among others [20–28]. In this work we present a continuation of our first efforts to increase the efficiency of sonochemical reactors [29]. The concept is based on small predefined crevices in which stabilized gas pockets remain entrapped when introduced into the liquid [30–33]. When exposed to ultrasound, these gas pockets continuously generate chemically active cavitation bubbles at their location. These bubbles form peculiar and stable clouds in the reactor that do not occur in the absence of the pits.

A major advantage of this method is that the location of the bubbles is stable, known a priori, and coincides with the region of high intensity ultrasound. This feature is in contrast with the usual sonoreactors where bubbles occur randomly over large volumes. The reproducible cavitation structures generated in our system enable us to study the relation between the bubble size distribution, number of bubbles, spatial distributions and chemical production rates. The latter are determined using dosimetry of OH<sup>•</sup> radicals while the former are obtained using a nanosecond flash-photography technique. In this paper, the acquired rates in terms of radical production per bubble per acoustic cycle are discussed. Additionally, calculations provide further insight into some of the observed phenomena.

\* Corresponding author. Tel.: +31 53 489 2594.

E-mail address: [d.fernandezrivas@utwente.nl](mailto:d.fernandezrivas@utwente.nl) (D. Fernandez Rivas).

<sup>1</sup> These authors contributed equally to this work.

## 2. Material and methods

### 2.1. Silicon micromachining

The bubbles were generated from the gas entrapped in pits with a diameter of 30  $\mu\text{m}$  and a depth of 10  $\mu\text{m}$  etched in square silicon chips with a side of 10 mm. These substrates were micromachined under clean room conditions on double-side polished silicon wafers with (100) crystallographic orientation. The pits were etched by means of a plasma dry-etching machine (Adixen AMS 100 SE, Alcatel). Pits arranged in three different configurations were used: single pits, two pits separated by a distance of 1 mm, and three pits arranged at the corners of an equilateral triangle with sides of 1 mm (see Fig. 1).

### 2.2. Set-up for US experiments and imaging technique

A sketch of the experimental arrangement is shown in Fig. 2. The cavitation cell was a glass container of 25 mm outer diameter, 15 mm inner diameter and 6 mm depth. The thickness of the cell bottom was 6 mm and matched one quarter of the wavelength at the operation frequency of  $200 \pm 5$  kHz generated by a piezo Ferroperm PZ27 6 mm thick and 25 mm in diameter glued to the cell bottom. To prevent loss of water by evaporation and gas by acoustic degassing the cell was covered by a glass slide resting on a rubber ring.

Two types of experiments were conducted, the measurement of sonochemical reaction rates and the imaging of the bubbles and their size distribution. For the first type, the acoustic excitation was a sinusoidal signal provided by a Hewlett Packard 33120A arbitrary waveform generator amplified by means of a SONY TA-FB740R QS amplifier. The voltage and current provided to the piezo were measured with a Tektronix DPO 4034 oscilloscope and Tektronix current probe CTA2. The bottom surface of the piezo was kept in contact with a Peltier element (Marlow Industrial) to maintain the temperature at a constant value of 25  $^{\circ}\text{C}$ . At low and medium power the temperature increase during each experiment was measured to be no more than 1 K, while in the high-power case the temperature increased no more than 3.8 K, mainly during the first minute, and then remained constant. To study the radical production three different power settings were used with all three pit arrangements: low (0.074 W), medium (0.182 W) and high (0.629 W).

The arrangement was similar for the bubble imaging experiments except for the use of a Krohn-Hite model 7602 wide-band amplifier and a Tabor Electronics Ltd. model WW1072 function generator. The different amplifiers resulted in differences in the electrical power supplied to the piezo element, which were 0.194 W (low), 0.654 (medium) and 0.981 W (high). In this case space constraints prevented the use of the Peltier element.

Imaging was carried out with two cameras, one Photron model SA1.1 recording movies at normal speed (25 fps), the other one used for single snapshots was a Lumenera LM165 with a sensitive Sony EXview HAD CCD sensor. The Olympus microscope was equipped with two long working distance (WD) objectives, the LMPLFLN10 $\times$ , (WD 21 mm/NA = 0.25) and the SMPLFLN20 $\times$  (WD 25 mm/NA = 0.25) both Olympus. Illumination was provided by a bright laser induced fluorescence pulse of 7 ns duration (full width at half maximum) which, amounting to about one thousandth of the acoustic period, enabled us to obtain high-resolution images without motion blur. The minimum radius detectable in the experiment was  $\sim 0.5$   $\mu\text{m}$ . Additional details on this method can be found elsewhere [34]. Examples of the images obtained in this way are shown in Figs. 3 and 4.

The purpose of these images was to obtain information on the number and sizes of the bubbles at various phases of the sound excitation. The difficulty to overcome was that the bubble density was high so that in many cases the images of different bubbles overlapped. To identify the individual bubbles it was therefore necessary to develop a special Matlab-based software using the so-called watershed segmentation algorithm [35]. After identification, the bubbles were counted and the image of each bubble was processed to extract the projected area and, with the assumption of a spherical shape, the equivalent diameter.

### 2.3. Pressure amplitudes

The quantity of interest for bubble oscillations is the acoustic pressure amplitude rather than the electrical power provided to the transducer. Unfortunately the conversion from one to the other is a notoriously difficult step. We attempted to measure the acoustic pressure amplitude by using a hydrophone (Onda HNR-500) with the tip positioned 65  $\mu\text{m}$  above the center point of the chip. The estimated error affecting these values according to the manufacturer is 20%. The values found in this way were 165 kPa for 0.074 W, 225 kPa for 0.182 W, and 350 kPa for 0.629 W. These values are uncertain due to several possible factors, electrical interference, the presence of waves on the surface of the liquid, bubble formation at the hydrophone tip and others. Furthermore, bubbles detune the cell and shield each other, therefore these values are provided only for reference purposes. A better estimate will be derived in Section 3.5 with the aid of numerical simulations.

### 2.4. Radical dosimetry

Conversion of terephthalic acid to 2-hydroxyterephthalic acid (HTA) was taken as a measure for the concentration of  $\text{OH}^{\cdot}$  radicals. A calibration graph of fluorescence intensity as a function of HTA concentration was obtained following steps similar to those described in the literature [36]. Fluorescence was measured using a

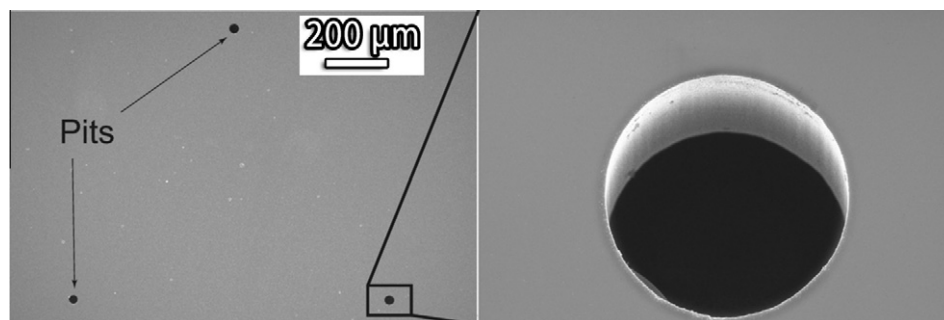


Fig. 1. Pits micromachined on a silicon substrate by deep reactive ion etching. Top view (left) and a zoomed-in perspective view (right). The diameter of the pit on the right is 30  $\mu\text{m}$ .

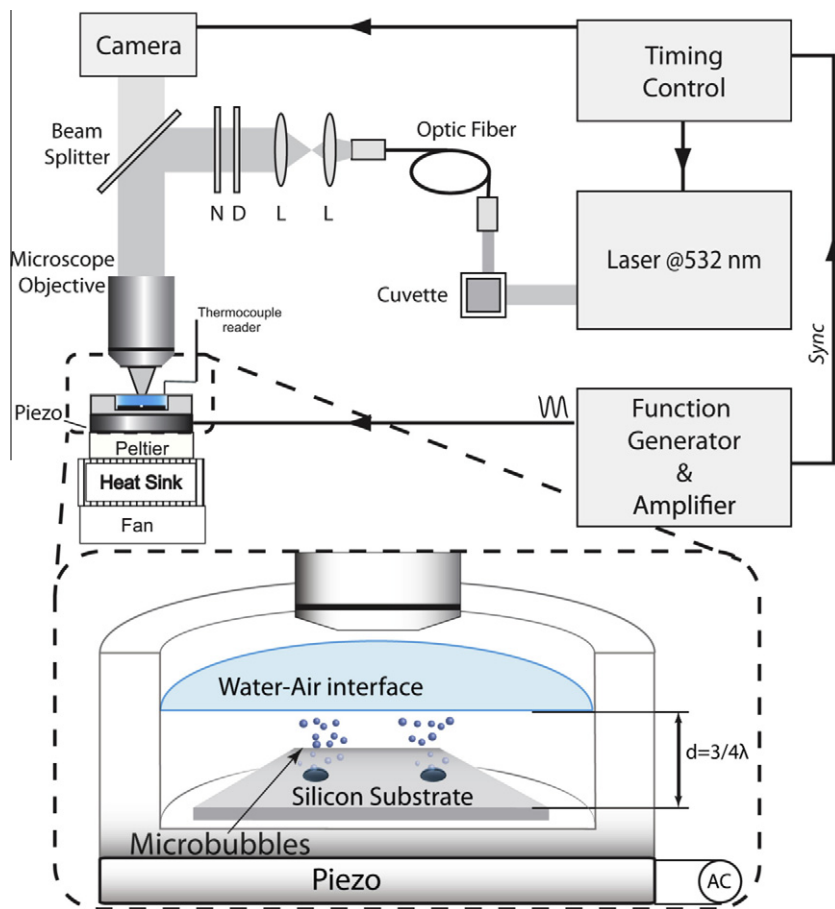


Fig. 2. Experimental setup used for short exposure imaging and inset showing a detailed sketch of the cavitation cell.

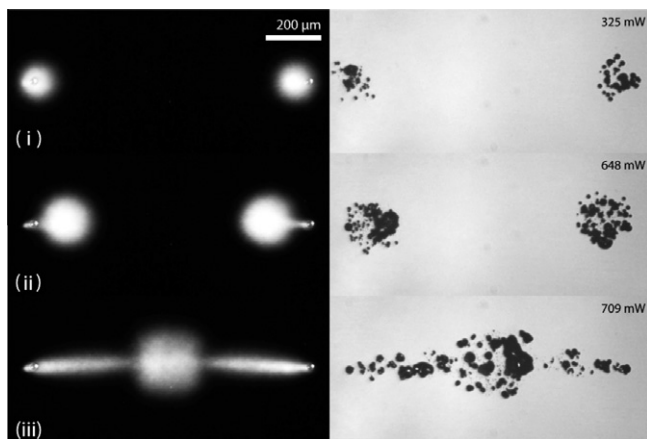


Fig. 3. Bubble clouds originating from a two-pits substrate. Each row corresponds to a different acoustic amplitude increasing from top to bottom. The left column illustrates the time averaged extent of the cavitation cloud imaged at normal speed. The right column are single snapshots of 7 ns exposure time, in which individual bubbles can be distinguished at approximately maximum expansion.

spectrofluorometer (TECAN Sapphire<sup>2TM</sup>) with an excitation wavelength of 310 nm. The fluorophore had a peak emission wavelength of 429 nm, but the emission was scanned between 350 and 600 nm. Following the method reported by Iida [37], the acid solution was prepared by mixing  $2.0 \times 10^{-3} \text{ mol/l}$  (0.332 g) of terephthalic acid (Sigma–Aldrich)  $5.0 \times 10^{-3} \text{ mol/l}$  (0.200 g) of NaOH and phosphate buffer (pH 7.4), prepared from  $4.4 \times 10^{-3} \text{ mol/l}$

(0.589 g) of  $\text{KH}_2\text{PO}_4$  and  $\text{Na}_2\text{HPO}_4$  ( $7.0 \times 10^{-3} \text{ mol/l}$  (0.981 g)) (all from Riedel - de Haën). The resulting solution was then made up to 1 l with milliQ water.

An amount of 300  $\mu\text{l}$  of the solution measured with an Eppendorf micropipette was used in each experiment. At the end of the experimental run, the solution was pipetted out of the cell and stored in dark in sterilized vials (manufactured by Brand) for spectroscopic analysis. This step was conducted with 200  $\mu\text{l}$  taken from the stored solution pipetted into the wells of a Corning Inc. well assay plate. The spectrophotometer settings for the analysis of the samples were: gain 40, height from the well, 9000  $\mu\text{m}$ , integration time 100  $\mu\text{s}$ , 10 reads per well.

Each experiment was repeated six to ten times and the mean concentration value was calculated. The largest standard deviation occurring for the case of three pits at maximum power, was about 30 % of the average value.

Calculation of the radical formation rate was carried out according to:

$$\frac{\Delta N_{\text{rad}}}{\Delta t} = \frac{(c_{\text{end}} - c_{\text{initial}}) N_A V}{\Delta t}, \quad (1)$$

in which  $c_{\text{end}}$  and  $c_{\text{initial}} = 0$  are the final and initial concentrations of HTA in moles per volume,  $N_A = 6.02 \times 10^{23} \text{ mol}^{-1}$  is Avogadro's number and  $V$  is the liquid volume exposed to the US (300  $\mu\text{l}$ ).

### 2.5. Theoretical bubble dynamics and radical production calculation

The model used to theoretically describe the bubble dynamics is based on an extended Rayleigh–Plesset-type equation, adopting the boundary layer approximation to estimate diffusive and thermal

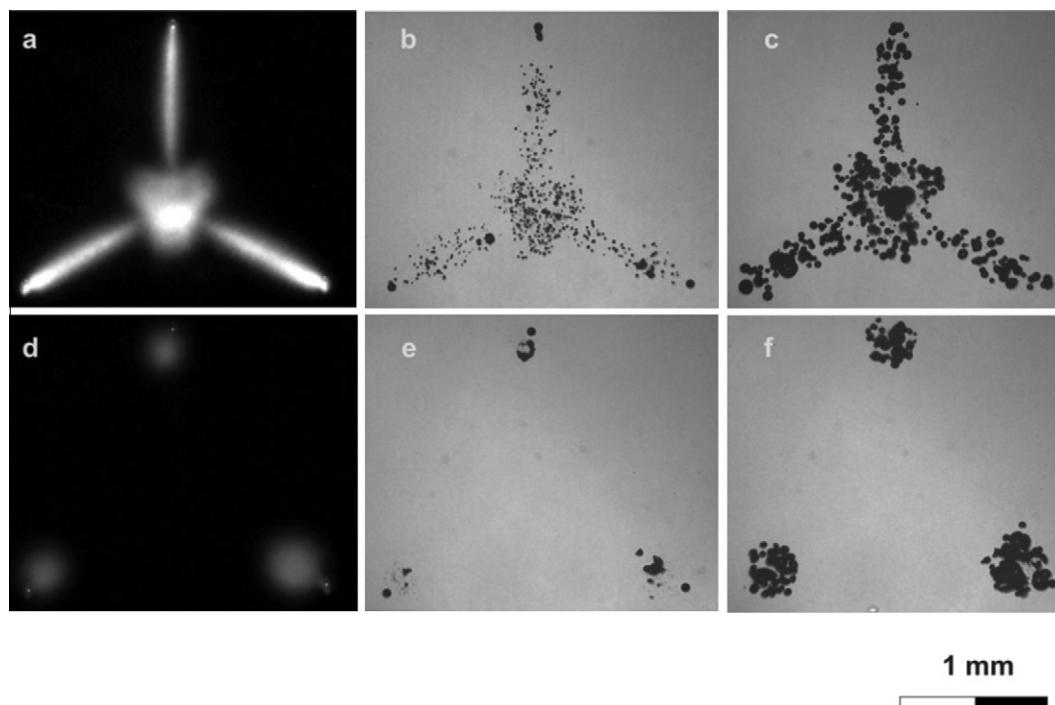


**Fig. 4.** Images of a substrate with three pits at different powers and at two selected points in the acoustic cycle. The upper row corresponds to high power (0.981 W) and the lower row to low power (0.194 W) with normal illumination conditions (a and d) and corresponding short exposure images: b and e in the compression; c and f in the expansion phase of the acoustic cycle.

fluxes and assuming spherical symmetry for the bubble [38–41]. Temperature evolution over time is given by a global energy balance. The gas inside the bubble is taken as air with a van der Waals type equation of state. Changes in the transport parameters in accordance with compositional changes of the mixture are also included in the model. A driving frequency of 200 kHz was taken, in agreement with experiments. Interaction between bubbles due to Bjerknes forces as well as coalescence effects were neglected.

### 3. Results and discussion

#### 3.1. Description of the observed phenomena

When the US is switched on, a continuous generation of bubbles is observed issuing from the gas stabilized in the pits on the silicon surface. These bubbles are likely caused by an instability of the liquid free surface at the pit mouth which undergoes large-amplitude oscillations under the action of the US. A similar process taking place at the surface of a free bubble has been described in the literature [42,43,7].

The resonance frequency of the pits is of the order of 150 kHz and the radius of bubbles resonating at the applied frequency of 200 kHz is about 15  $\mu\text{m}$  [44,45]. Thus one would expect that, under the action of Bjerknes forces, bubbles smaller than this size would be repelled by the pits while larger ones would be attracted. At low power, the observed behavior is compatible with this expectation as shown in Figs. 3 and 4. A few bubbles are observed at any given time. They move some distance away from the pit and survive a few cycles before disappearing [44].

As the power is increased, the ejected bubbles become more numerous forming clouds of increasingly larger size around the pits. At still higher powers, with more than one pit, the clouds appear to be attracted to each other until, at a fairly reproducible power level, they travel towards the central area of the pit array where they collect forming a single cloud (see Figs. 3 and 4). As shown in an earlier paper [29], and as can be seen in the last frame

of Fig. 8 below, these clouds when observed from the side resemble the conical clouds formed at the tip of sonotrodes [46,47]. These structures are very different from the filamentary structures, sometimes called acoustic Lichtenberg figures [48], which are common in normal acoustic cavitation at high acoustic amplitudes.

The cloud is continually fed by new bubbles arriving from the pits under the action of the complex interplay of primary and secondary Bjerknes forces and micro-streaming acting on the bubbles. The bubbles in the cloud are observed to break up seeding the liquid with their fragments which then grow into additional bubbles that join the cloud. The processes responsible for the accretion and loss of bubbles eventually reach a steady state and the cloud is not observed to grow further.

The transition from clouds localized near the pits to a central cloud exhibits hysteresis, with the pressure amplitude necessary to return to separated clouds lower than that needed to bring them together.

The three-pits arrangement of Fig. 4 shows transition to a pattern similar to that of Fig. 3 for two pits when one of the three pits is rendered inactive (see Fig. 5). This observation suggests that

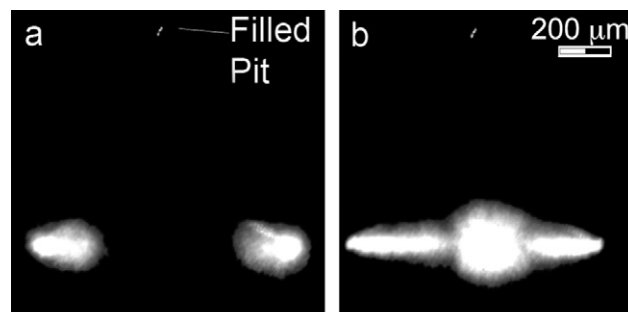


**Fig. 5.** When a pit is filled with water in a three-pit substrate, the bubbles nucleated by the remaining active pits attain the same configuration as for a two-pit substrate: (a) Medium power (0.654 W) and (b) High power (0.981).

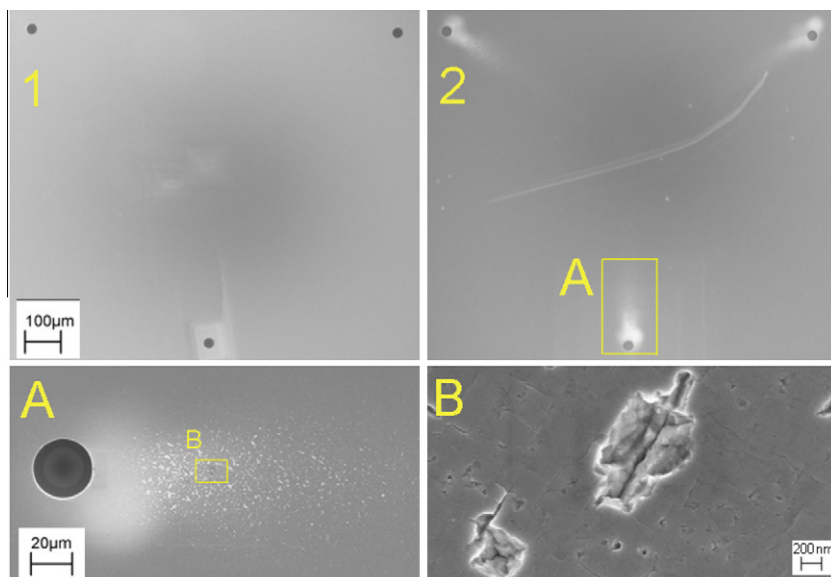


**Fig. 6.** SEM image affording a comparison of a substrate before (1) and after (2) use in ultrasonic experiments. The damage pattern and zoomed-in views of it show that the eroded surface coincides with the {111} silicon crystal planes.

liquid flow does not play a major role in the observed cloud attraction, which therefore must be mostly due to Bjerknes forces.

At high power a region of damaged silicon substrate forms near the pits within 5 min of exposure to the US (see Fig. 6). The shape of the individual damage sites coincides with the crystal planes of the crystalline structure of the silicon wafers. Damage to other

parts of the chip and, in particular, under the large cloud forming over the center of the pit array, is much more modest and takes a significantly longer time.

We have found that this localized acoustic bubble generation can be sustained for at least several hours if temperature is kept constant and gas loss is prevented by means of the glass slide mentioned before. Therefore we must conclude that the loss of gas associated to the bubble generation does not deactivate the pits, which is evidence of a process of rectified gas diffusion into the pits similar to the well-known process taking place with free bubbles.

The emission of shocks by collapsing bubbles is a known feature [49,50]. An example in our case is shown in Fig. 7.

When bubbles are close to each other or to the solid surface, which preferentially occurs at higher power, they tend to deform and to interact. When bubbles are close enough, they develop liquid jets towards each other (see as an example [51]). Fig. 8 shows several examples of such deformations and interactions.

In interpreting these images it must be kept in mind that bubbles smaller than resonance size expand during the acoustic compression phase, while bubbles bigger than resonance size contract. At high powers these latter bubbles may become unstable and split, generating the significantly smaller bubbles seen in the figure. The actual stability of these bubbles will also be influenced by their distance from the solid substrate and the proximity of other bubbles. Some of the smaller bubbles may also become unstable and fragment during collapse, but this would happen during the acoustic expansion phase.

We have estimated the translational velocity of typical bubbles on the basis of some preliminary experiments by imaging the acoustic field at 1.4 Mfps. We found typical velocities of about 10 m/s and corresponding lifetimes of 100  $\mu$ s, which is of the same order as that reported for other typical sonoreactors at similar frequencies [18] where bubbles had a lifetime of the order of 350  $\mu$ s.

### 3.2. Bubble size distribution

As explained before, in order to characterize the bubble size distribution and its evolution in time over an acoustic period, we took snapshots of the cavitating region with an exposure of 7 ns. The repetition time of the laser did not allow us to take consecutive

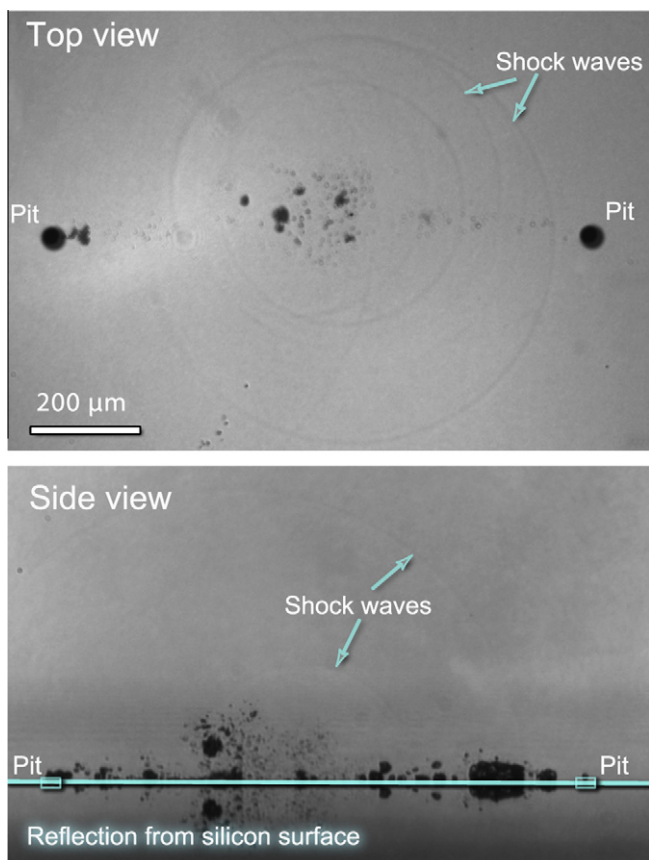


**Fig. 7.** Shock waves emitted in the two-pit, high power situation (0.981 W). Several shock waves are observed in top and side views.

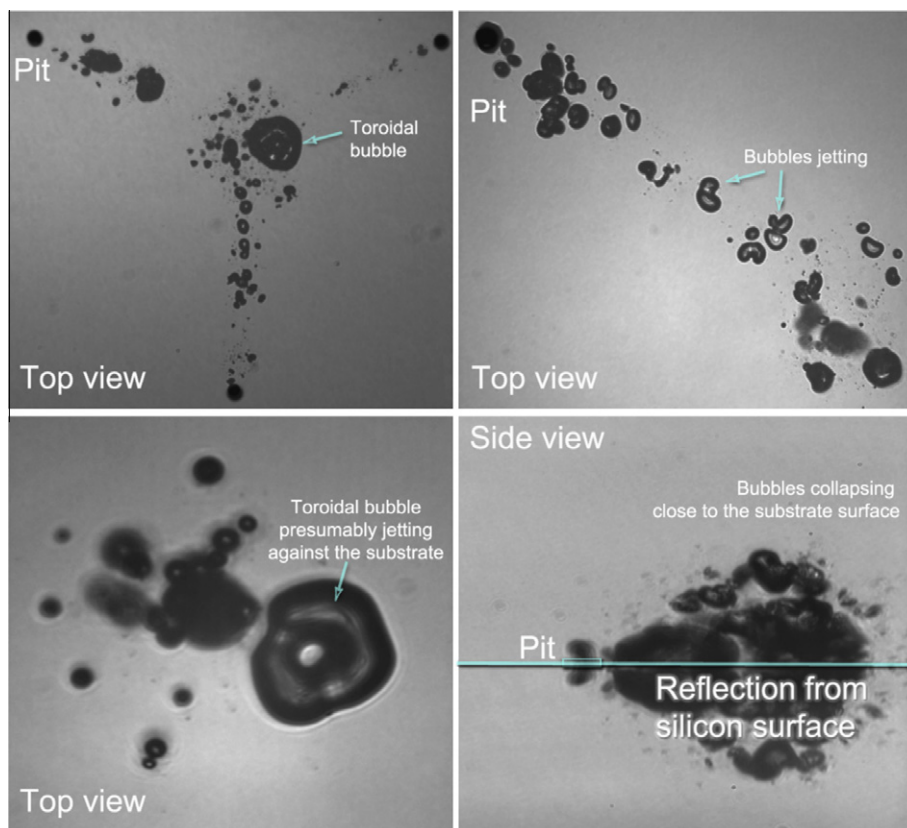


**Fig. 8.** Deformed bubbles at high power settings (0.981 W). Note how bubbles tend to deform in all cases. When two bubbles are close, they develop liquid jets towards each other as in the upper right picture.

images faster than about 1 per second, i.e., every 200,000 acoustic cycles. The laser timing was set so as to generate a flash at a fixed phase of the sound field. We selected 10 phases and took 10 images per phase to improve the statistics.

As shown in Table 1, at the low power settings the number of bubbles in each frame was relatively small, typically 3–5 per pit and sometimes even less. Furthermore, the occasional overlaps of the bubble and pit images made it difficult to accurately count these bubbles. The measured low-power bubble populations, therefore, are not very accurate but are presented for reference as a lower bound; an example is provided in Fig. 9.

At the medium power settings the statistics improves since the bubbles tend to be more numerous, to grow larger and to move away from the pits. An example of a PDF for medium power is shown in Fig. 10.

**Table 1**  
Bubble population characteristics in a cycle

	1 pit	2 pits	3 pit
<i>Low power (0.194 W)</i>			
Most probable radius [ $\mu\text{m}$ ]	17	3	2
Average bubble radius [ $\mu\text{m}$ ]	16	10	12
$N_{\text{bubble}}$	3	5	17
<i>Medium power (0.654 W)</i>			
Most probable radius [ $\mu\text{m}$ ]	2	3	3
Average bubble radius [ $\mu\text{m}$ ]	9	12	8
$N_{\text{bubble}}$	4	29	113
<i>High power (0.981 W)</i>			
Most probable radius [ $\mu\text{m}$ ]	2	3	5
Average bubble radius [ $\mu\text{m}$ ]	8	9	10
$N_{\text{bubble}}$	50	102	96

At high power (0.981 W) and one-pit configuration the expansion and collapse of the ejected bubble are very dramatic and their shape is highly deformed. The equivalent radii, therefore, are less representative of the actual size of a corresponding spherical bubble. The number of bubbles can also be under-estimated since some large bubbles overlap and the post-processing code can consider two or a blob of several bubbles as a single one. Nevertheless it provides a qualitative measure of their number. A typical PDF for high power is depicted in Fig. 11.

The bubble size distribution for a certain acoustic phase is the distribution of equivalent radii of the total number of bubbles over the 10 frames taken at that phase. The average radius is obtained by averaging the radii of all the bubbles in the 10 frames and the most probable radius is that with most occurrences at that phase. For example, a bubble size distribution such as that in Fig. 11 for  $t/T = 0$  is right-skewed i.e. more frequent smaller equivalent radii (R). The most probable radius is  $\sim 2 \mu\text{m}$ , but the average radius is larger, as the distribution includes a range of radii up to  $35 \mu\text{m}$ . See Fig. 12 for more details.

Table 1 presents a compilation of the experimental data on several measures of bubble size and average number per cycle. As noted above, the radius of resonant bubbles at the experimental frequency is about  $15 \mu\text{m}$ . The measured average bubble radius is of this order (8 to  $16 \mu\text{m}$ ) and the most probable radius is between 2 and  $5 \mu\text{m}$ . Fig. 12 shows an example of the evolution of the most probable and average radii, together with the number of bubbles during one acoustic cycle at 0.981 W for three pits. It is seen in the bottom panel of this figure that the number of bubbles peaks shortly after the maximum pressure. This feature may reflect the expansion of the smaller bubbles which are below the optical resolution of our apparatus during the rest of the acoustic cycle.

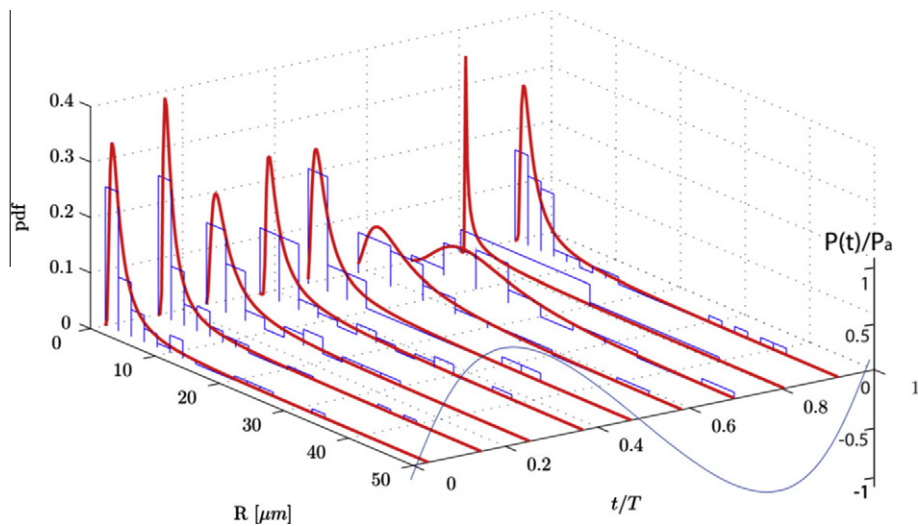


Fig. 9. Bubble size distribution histograms at a power of 0.194 W for one pit. The axis to the extreme right represents the normalized pressure for the acoustic cycle.

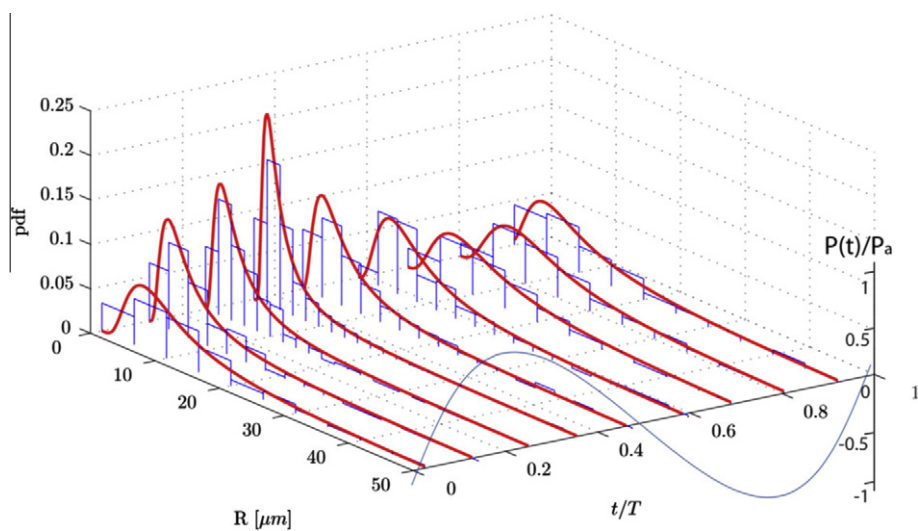


Fig. 10. Bubble size distribution histograms for a power of 0.654 W for two pits. The axis to the extreme right represents the normalized pressure for the acoustic cycle.

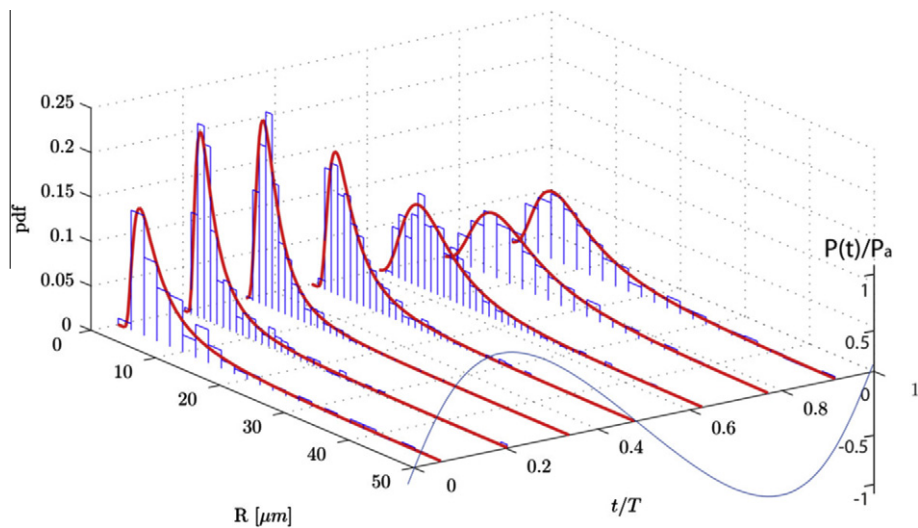
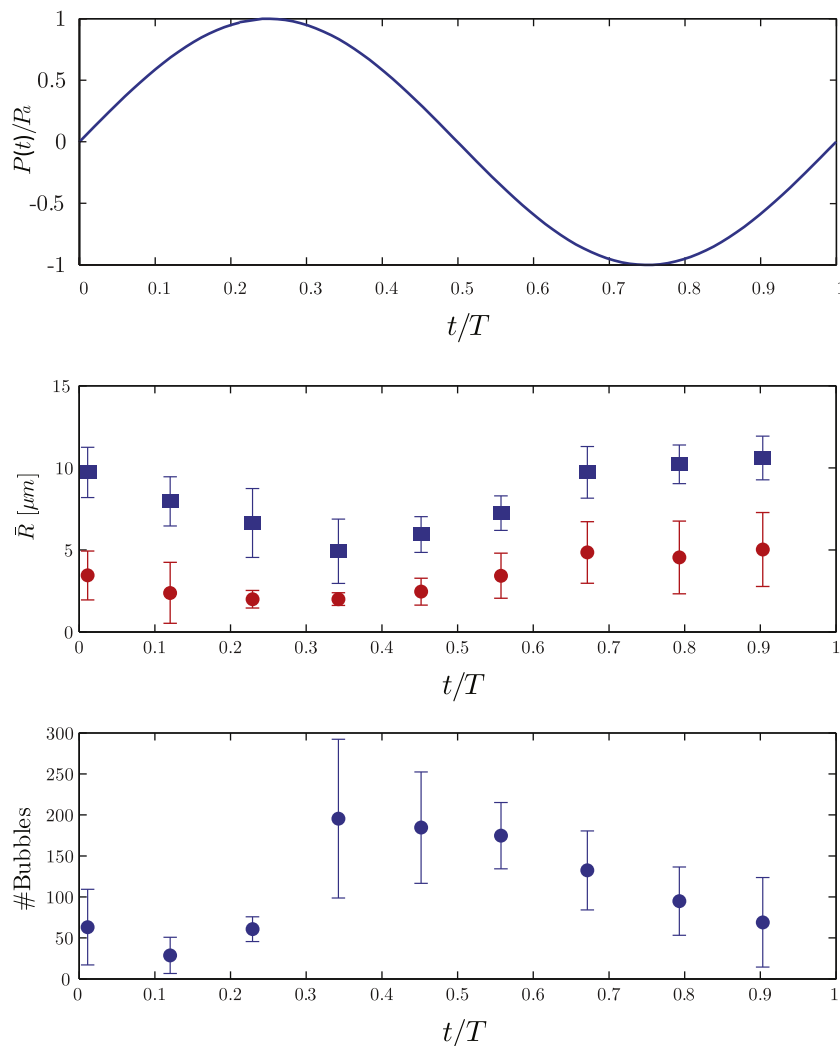
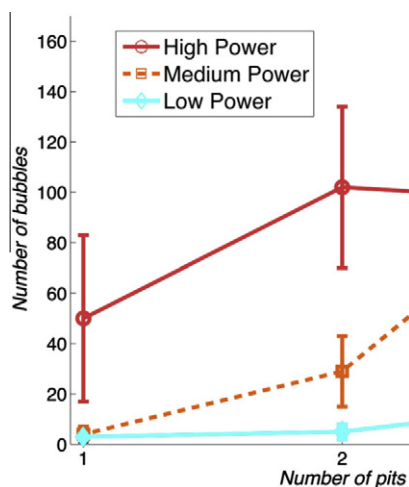


Fig. 11. Bubble size distribution histograms at a power of 0.981 W for three pits. The axis to the extreme right represents the normalized pressure for the acoustic cycle.



**Fig. 12.** Top: normalized pressure for the acoustic cycle. Center: most probable radius (circles) and average radius (squares); Bottom: average number of bubbles at different phases at a power of 0.981 W for three pits.



**Fig. 13.** Average number of bubbles in the cavitation field for the different power settings: low (0.194 W), medium (0.654 W) and high (0.981 W).

The average number of bubbles instantaneously present is shown in Fig. 13. These data were obtained by summing the number of all bubbles visible in all frames (10 frames each for 10 phases) and dividing by a hundred. For the one-pit configuration,

as the power is increased the number of bubbles increases as would be expected. The results shown for low and medium power correspond to isolated bubble clouds while for two and three pits at high power the clouds have merged as explained before. When this happens, the observed bubble number does not increase, possibly due to bubble–bubble interactions and the finite amount of gas available [52–54].

### 3.3. Experimental radical production rates

It was shown earlier [29] that the duration of the experiment does not seem to affect the reaction rates up to 30 min of operation. The radical production rate defined in Eq. 1 is shown as a function of the ultrasonic power in Fig. 14. It is important to note that there is no significant effect of the US power when no pits are present. It is clear that the presence of the pits is essential for the generation of sonochemically active bubbles: the pits enhance cavitation by facilitating the appearance of a larger number of bubbles, at a location in the reaction cell that otherwise would have no detectable bubbles or none at all.

For the lowest power the total radical production rates are around  $5 \text{ nM s}^{-1}$ , but as the power is increased, the reaction rate increases as well. The maximum value corresponds to the three-pits configuration at high power.

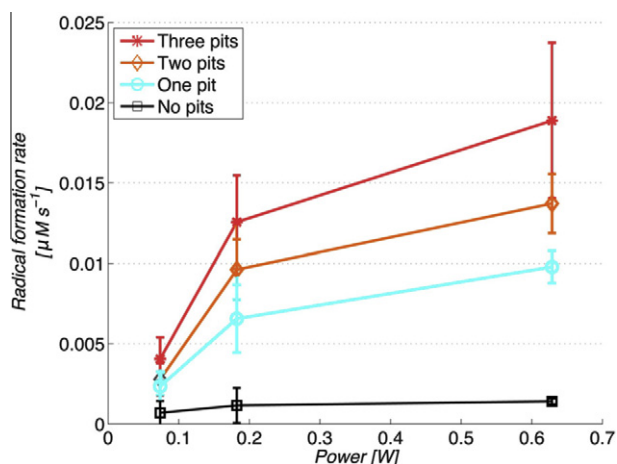


Fig. 14. Radical production rates for the different power settings.

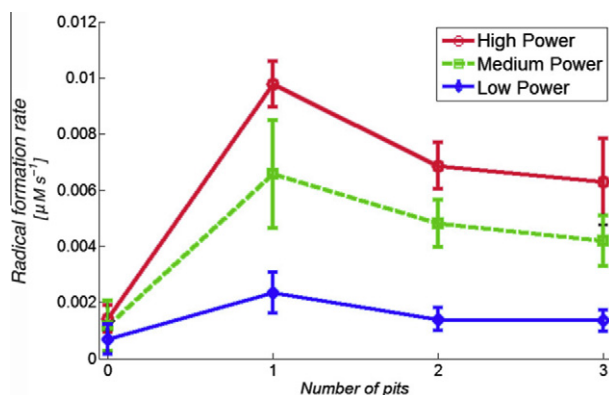


Fig. 15. Radical production rates for the different power settings (low, 0.074 W, medium, 0.182 W and high, 0.629 W) divided by the number of pits.

When the amount of radicals formed per second is divided by the number of pits we see an interesting trend depicted in Fig. 15. For one pit the rate of radical formation is higher than for two- and three-pits in all cases. Possible factors contributing to this result are the mutual shielding of the bubbles, a detuning of the cell and change in the sound power distribution due to the larger gas volume fraction, the availability of dissolved gas in the liquid and possibly others.

If we calculate the radical production per cycle and divide it by the average number of bubbles per cycle, we can get an estimate to be compared with single bubble radical production measured by Didenko and Suslick [6] who reported data for a single bubble of maximum radius of 28.9  $\mu\text{m}$  driven at 52 kHz. They measured an  $\text{OH}^\cdot$  radical generation rate of  $6.6 \times 10^5$  per cycle. Our data, which are shown in Table 2, are of the same order of magnitude despite the differences in the experimental parameters. We expected lower rates due to the smaller volume of our bubbles (itself a consequence of the higher frequency), to mutual shielding and bubble

Table 2  
Radical production per detected bubble per cycle

	1 pit	2 pits	3 pit
Low power (0.074–0.194 W)	$7.06 \times 10^5$	$5.03 \times 10^5$	$2.15 \times 10^5$
Medium power (0.182–0.654 W)	$1.48 \times 10^6$	$2.99 \times 10^5$	$1.00 \times 10^5$
High power (0.629–0.981 W)	$1.76 \times 10^5$	$1.21 \times 10^5$	$1.78 \times 10^5$

deformation. A possible explanation for our results is radical production by bubbles smaller than 0.5  $\mu\text{m}$ , which our experimental technique cannot resolve.

### 3.4. Discussion of the calculated efficiencies

In principle, a measure suitable for the quantification of the sonochemical conversion could be defined as:

$$X_{US} = \frac{\Delta H(\Delta N_{rad}/\Delta t)}{P_{US}}, \quad (2)$$

where  $P_{US}$  is the power absorbed by the transducer and  $\Delta H$  is the energy required for the formation of  $\text{OH}^\cdot$  radicals (5.1 eV =  $8.2 \times 10^{-19}$  J), which is equal to the enthalpy of formation associated with the following chemical reaction:



The problem with this definition is that only a small fraction of the power provided to the piezo is responsible for the sonochemical effect [55]. As a matter of fact, by comparing the power absorbed with and without pits and, therefore, in the presence or absence of intense bubble activity, we have found very small differences. This leads us to conclude that the majority of the power absorbed by the system is lost in the electrical-to-mechanical conversion. Nevertheless we will use the definition (2) as a convenient dimensionless measure of the sonochemical conversion efficiency. The electric power absorbed by the transducer  $P_{US}$  was determined from the measured voltage and current, and their phase difference.

The efficiency values calculated with Eq. (2) are shown in Fig. 16. As presented before [29], the most efficient settings appears to correspond to medium power. However, for the reasons mentioned before, the efficiencies shown in the figure may not reflect purely acoustic features of the system. Nevertheless we present this data following the prevailing custom in the sono-chemical literature [55,27].

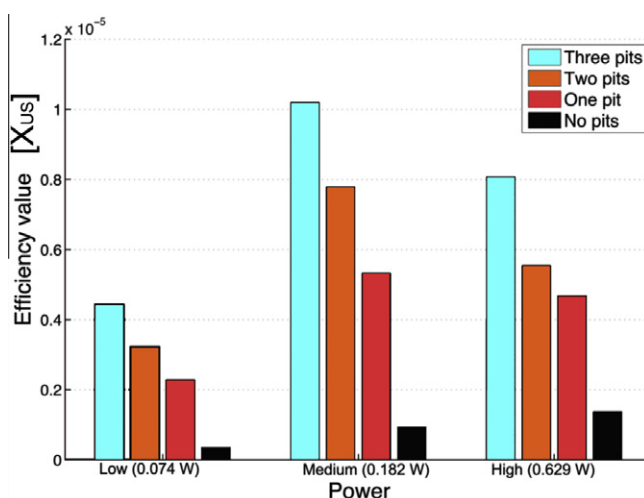
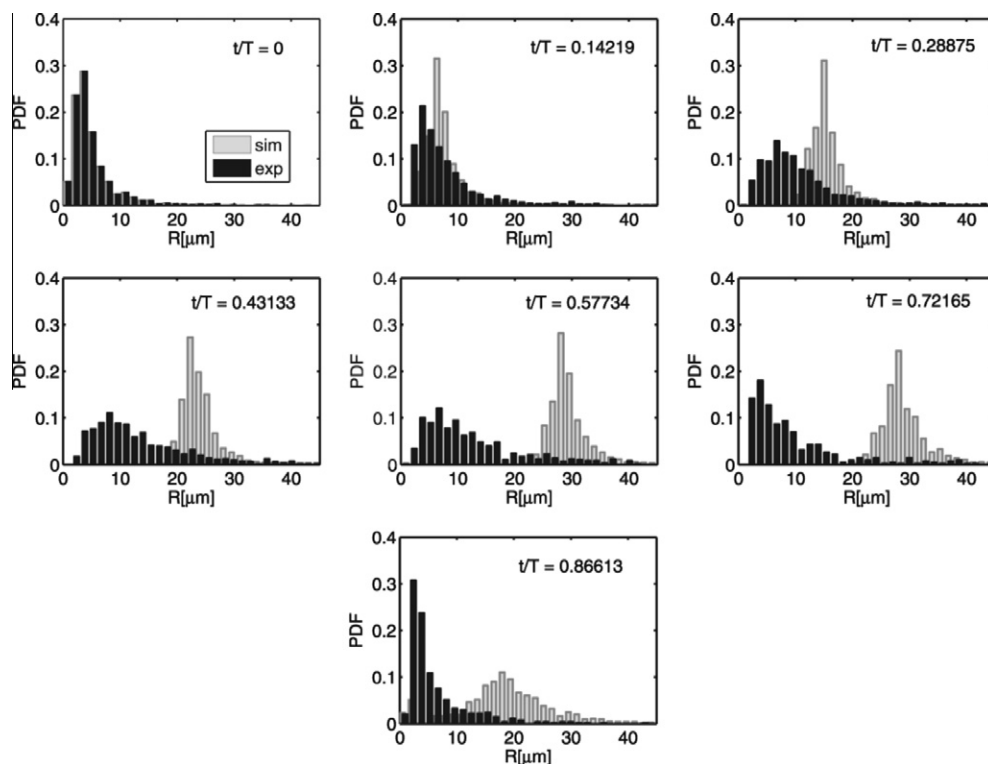


Fig. 16. Nominal experimental efficiency values ( $X_{US}$ ) for different number of pits and different US powers calculated from Eq. (2). The presence of pits for each power makes a clear difference with an increase in efficiency as the number of pits is increased. In the case of no pits, an increase in power produces a slow increase in efficiency. From low to medium power the trends increase for any number of pits. For the high power case, there appears to be a decrease in efficiency for any number of pits. It is not clear whether this result corresponds to true differences in the acoustic and sonochemical processes or to a decreased efficiency of conversion from electrical to mechanical power.



**Fig. 17.** Bubble size distribution from experiment (black) and simulation (grey), for high power (0.981 W) and the three-pit configuration. It appears that the pressure amplitude measured with the hydrophone overestimated the effective value felt by the bubble population. Simulations carried out using these values were not able to describe the evolution in time of the radii distribution, as the average radius was overestimated during the whole cycle, the expansion phase was much longer than in experiments and the distributions were almost symmetric, instead of right-skewed.

### 3.5. Obtaining numerical effective bubble size distributions and effective driving pressures

As explained in Section 2.5, one can estimate the production of radicals in a single bubble on the basis of existing models. In order to apply these models to the complex bubble fields studied in the present experiments, it is necessary to know the distribution of bubble radii and the effective pressure amplitude to which each bubble is subjected.

For this purpose we relied on measured probability distributions of bubble sizes at each phase of the sound field. These PDF were obtained by collecting 10 snapshots of the bubble field for each phase of the pressure. Each snapshot can be considered as statistically equivalent and independent from the others as the separation between successive ones was  $2 \times 10^5$  cycles which is much longer than the expected lifetime of the individual bubbles. The idea of the simulation was to determine a pressure amplitude and bubble equilibrium radius distribution that matched the measured radii distribution at each phase.

We started from the measured distribution at a particular phase chosen so as to have a large number of bubbles, which generally coincided with a small average radius and small standard deviation. For each one of these bubble radii we integrated the extended Rayleigh-Plesset equation assuming a vanishing initial radial velocity and using different pressure amplitudes [38]. We found that the nominal pressure amplitudes applied in the experiment produced bubble size distributions quite different from the measured ones, as shown in Fig. 17.

In order to match the measured distributions (see Figs. 9–11) it was necessary to adjust the pressure amplitudes used in the simulations, which resulted in much lower values than the nominal experimental ones. The adjustment was done by minimizing the

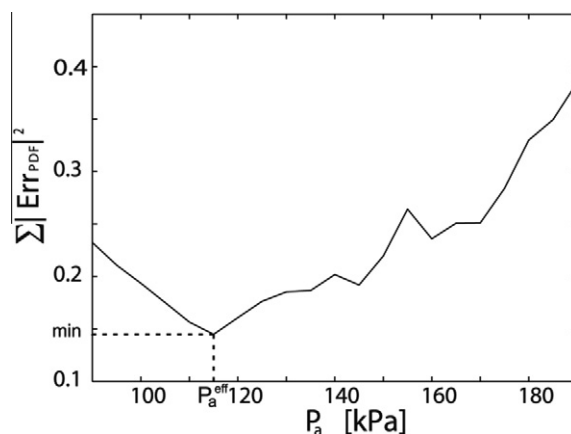


**Fig. 18.** Cumulative squared error (over all bubble sizes and acoustic phases) between the PDF of the radii from experiments and from the simulations, as a function of the pressure values used in the simulations, for three-pit configuration, at high power (0.981 W). The effective driving pressure felt by the bubble population was 115 kPa and was extracted by minimizing the cumulative squared error.

cumulative squared difference between experimental and calculated PDF for each phase (see Fig. 18).

The pressure levels deduced in this way were in the range between 110 kPa and 170 kPa. Since the minimum radius detectable in the experiment was about  $0.5 \mu\text{m}$ , a larger number of small bubbles appeared in simulations than in the experiment. The fit between experimental and calculated PDF was best for high applied power and more pits, i.e. for high numbers of nucleated bubbles (see Fig. 19 and 20).

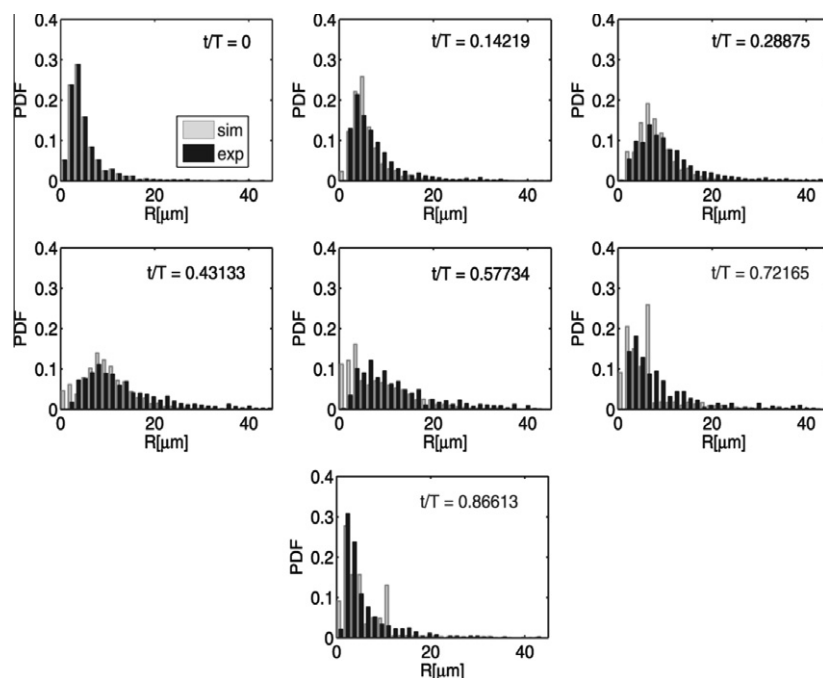


**Fig. 19.** Bubble size distribution from experiment (black) and simulation (grey), for high power (0.981 W) and the three-pit configuration. The effective pressure amplitude extracted of 115 kPa provided a good description of the dynamics of the system. The agreement between experiments and simulations was best for more pits and high applied power, i.e. for high number of nucleated bubbles. As expected, a higher number of small sized bubbles appeared in simulations than in experiments, as the minimum bubble radius that the experimental apparatus could detect was 0.5  $\mu\text{m}$ .

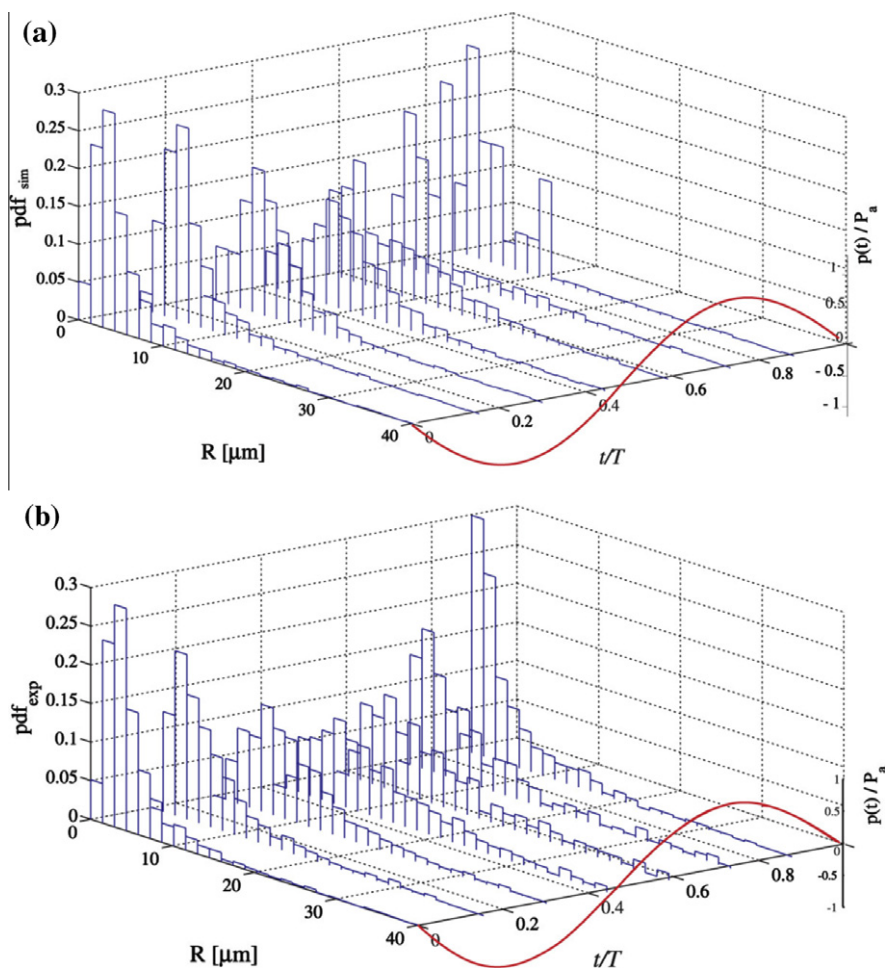


**Fig. 20.** Bubble size distribution histograms at high power (0.981 W) for three pits. From experiments (lower figure), and from simulations (upper figure) with the deduced effective pressure (115 kPa), which gives the best fit to the observed bubble distribution.

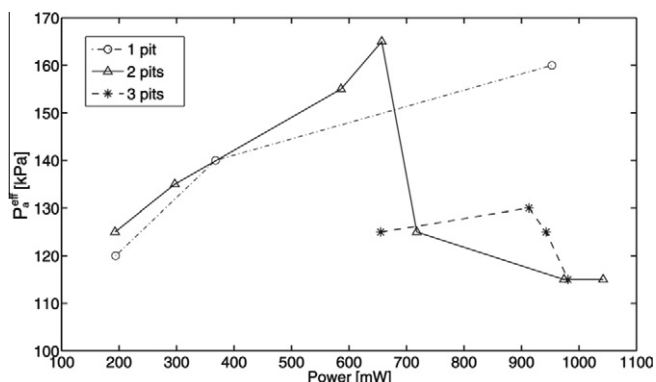


**Fig. 21.** Effective driving pressure felt by the bubble population as a function of the applied power. These values were derived from our fitting procedure between experimental and calculated PDF of the radii (see Fig. 18). For different number of pits, bubbles started to appear for different applied powers in experiments, although corresponding to the same deduced effective pressure (around 125 kPa). In the one-pit configuration, the effective pressure monotonically grew with the electric power. In the two- and three-pit cases the effective pressure initially had a similar behavior, but it abruptly decreased when the bubbles started to migrate towards the center point of the pit array above 0.657 W and 0.914 W respectively.

At low applied power the number of bubbles detected in the experiments was too small to provide good statistics, especially in the one-pit configuration. Moreover, at low power, the standard deviations of both the experimental and the calculated PDF normalized by the average radii were higher during the whole oscillation cycle, even if the average radii themselves were larger. This means that the data were more scattered than in the high power case, both in absolute and relative terms.

In the one-pit case, if we increased the applied power, the effective pressure derived from simulations monotonically increased (see Fig. 21) together with the number of bubbles measured in the experiments, while their average radii and normalized standard deviations decreased. In the two- and three-pits cases, a similar behavior was observed, with the effective pressure rising with the applied power and the average radius decreasing.

This trend, however, changed in correspondence of the pressure levels at which the observed bubble distribution switched from separate clouds surrounding each pit to the complex bubble field structure observed in Fig. 3 and Fig. 4. Beyond this threshold, the measured bubble size distribution changed significantly and the pressure necessary to fit the data abruptly decreased. This supports our view that the mutual shielding of the bubbles leads to a reduction in the effective pressure seen by the bubbles.

### 3.6. Calculation of the radical production

On the basis of the bubble sizes and pressure amplitudes determined in the way described in Subsection 3.5, we calculated then the number of OH<sup>•</sup> radicals produced by single bubbles with the equilibrium radius corresponding to the experimental distribution.

The bubble population at the instant at which the average radius over the 10 frames was minimum was taken as the initial and equilibrium distribution for the simulations. This generally coincided with the instant when the highest number of bubbles was found.

For this calculation, one hundred equi-spaced bubble equilibrium radii were chosen for each 10 μm size bin. For the pressure conditions given by the fitting procedure, the number of radicals diffusing inside the liquid over the first cycle was calculated for each value of the radius. The results were then averaged over all the radii belonging to the same bin.

As a general behavior, the calculated chemical output was higher at higher effective pressure but, in the two- and three-pits

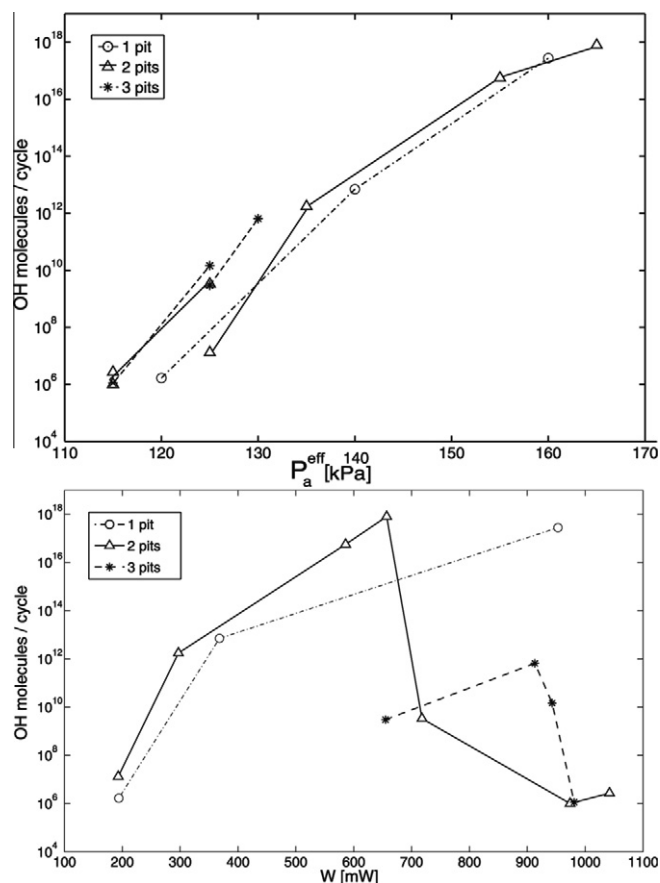


**Fig. 22.** Number of OH<sup>•</sup> radicals diffusing into the liquid, in each acoustic cycle, as a function of pressure (upper figure) and applied power (lower figure), both calculated from simulations. The calculated chemical production increased with the effective pressure, but also depended on the PDF of the radii. In the two- and three-pit cases, when the bubbles migrated towards the center point of the pit array (at 0.657 W and 0.914 W), more radicals were produced than when they remain near the pits, although the effective pressure was the same (125 kPa). In the upper figure this corresponds to the first branch of the two- and three-pit curves (below 125 kPa). The right branches correspond to the initial rise of the power.

configurations, the radical production exhibited a significant dependence on the bubble size distribution, which was different before and after the transition from individual bubble clouds to complex patterns. Thus, a higher radical production was observed in the latter cases even for the same calculated effective pressure (see Fig. 22).

The transition to the complex bubbles patterns affects the acoustic field and the liquid flow in the cell, with possible consequences for the sonochemical activity as found in earlier studies [56].

In all the cases examined the whole OH<sup>•</sup> radical production was found to come from bubbles smaller than resonance size, i.e. smaller than 15 μm, and mainly from those with a radius around 5 μm (see Fig. 23–25). In particular, higher effective pressure amplitudes resulted in smaller sizes of the bubbles giving the peak chemical production. This effect is dominant with respect to differences in bubble volume and the surface area of the bubble across which radicals diffuse.

The experimental rates span over one decade, while the theoretical rates shown in Fig. 22 span six decades. The reason for this is that the experimental precision is much lower than that of the numerical calculations, hence the strength of combining these two approaches.

It must be noted that our spherical bubble model overestimates the reaction rates measured in the experiments. This is perhaps not

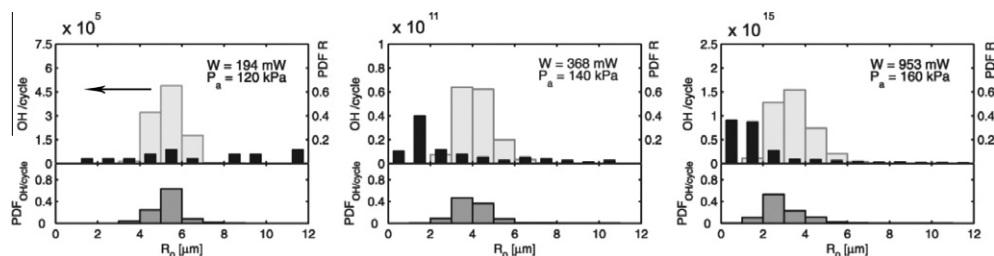


**Fig. 23.** One-pit case. Upper figures, light grey: calculated number of  $\text{OH}^\cdot$  radicals diffusing into the liquid at each acoustic cycle per bubble, as a function of the initial radius  $R_0$  for a single bubble (see Section 3.6 for the details). Upper figures, black: PDF of the initial experimental distributions of the radii in the one-pit case, for different applied powers. Lower figures, dark grey: PDF of the  $\text{OH}^\cdot$  radicals diffusing into the liquid in each acoustic cycle, as a function of the initial radius. These values were obtained by normalizing the number of the  $\text{OH}^\cdot$ /cycle produced by every bin of initial radii over the total number of  $\text{OH}^\cdot$ /cycle from the specific distribution. These lower figures can be seen as a combination of the two upper graphs. Simulations showed that the most radical production came from bubbles smaller than resonant size ( $15 \mu\text{m}$ ). In particular, higher effective pressure values corresponded to smaller sizes of the most active bubbles.

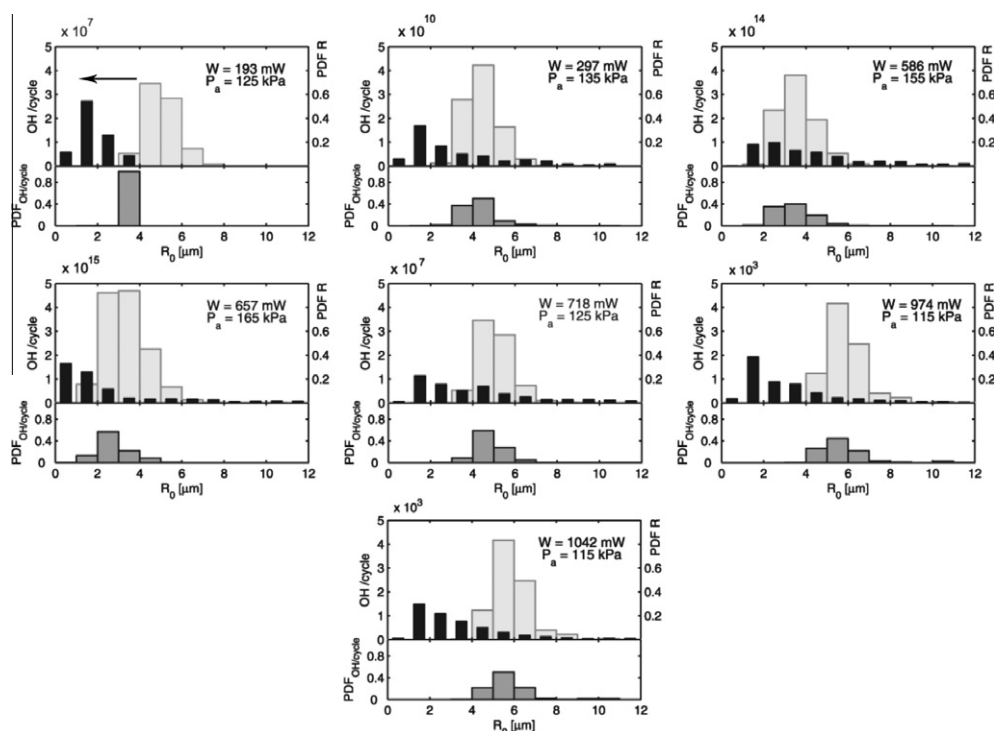


**Fig. 24.** Same as Fig. 23 for the two-pit case.

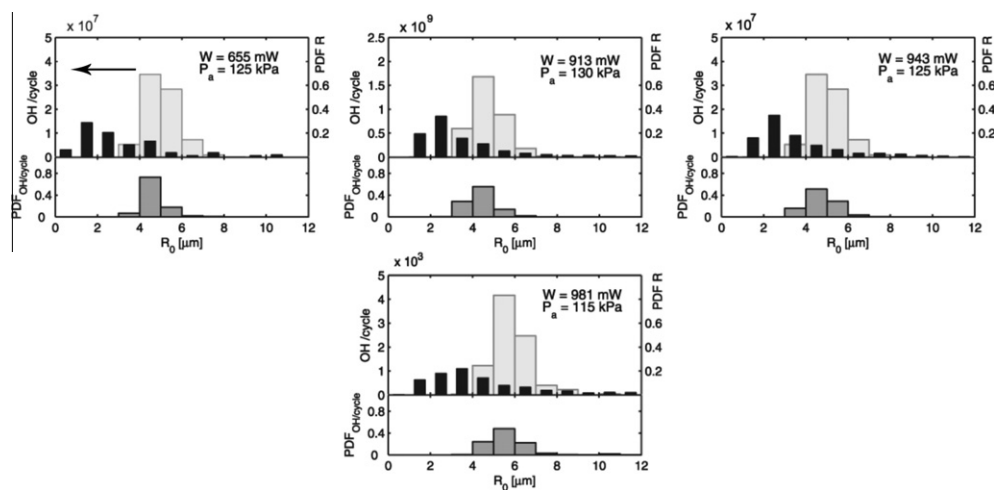


**Fig. 25.** Same as Fig. 23 for the three-pit case.

surprising given that the many factors that induce non-spherical collapse and therefore limit the compression of the gas are absent from the simulation. The simulations should be regarded as establishing an upper limit to the reaction rates. In principle, it may be thought that non-spherical bubble models could reduce the gap between simulations and experiments, although the complexity of the experimental situation will probably lie beyond any practical model in the foreseeable future.

#### 4. Summary and Conclusions

We achieved a more controllable and more efficient sono-reactor design by microfabricating small pits on a silicon chip immersed in a small sono-reactor of the ultrasonic bath type. Under the action of an ultrasonic field, the air trapped in the pits gives rise to a stream of small bubbles which are responsible for the intense sonochemical activity. A rectified diffusion process is responsible for replenishing the air and maintaining the activity of the pit.

We have shown that this modification of the solid surface yields considerably higher conversion rates. We have measured the bubble size distribution at different power settings and characterized its evolution during the acoustic cycle.

Simulations were carried out in order to give an estimate of the radical production in the different power settings. By fitting the experimental and the calculated PDF of the radii and minimizing the cumulative squared differences between the two, an estimate of the effective forcing pressure felt by the bubbles was found. In the two- and three-pit cases the effective pressure dropped when bubbles started to migrate towards the center point of the pit array. Simulations also allowed us to give a description of the temporal evolution of the smaller bubbles below 3  $\mu\text{m}$  radius, compatible with the experimental PDF. This turned out to be particularly relevant, as calculations showed that the most  $\text{OH}^\cdot$  radical production came from the smaller bubbles around 5  $\mu\text{m}$  radius. As a general trend, the calculated chemical rate increased monotonically with the effective pressure.

Even though the numerical model considers spherical bubbles without interaction, an important strength lies in the possibility of taking the actual experimental bubble size distribution (with its equivalent radius corresponding to non-spherical bubbles) and giving information on the smallest bubbles that are below the experimental observability. This computation can be considered as a useful complement to the experiment since it permits one to estimate the local pressure value to which the bubbles are exposed and which cannot be directly measured with the available pressure sensors.

It may be possible to extend the present surface modification to larger scale sono-reactors by supplying similar nucleation sites on larger surfaces and in a much greater number. As a guide towards the development and optimization of these types of reactors, it will be useful to investigate in greater detail several aspects such as pit density, dimensions, mutual interaction and many others.

#### Acknowledgments

We acknowledge S. Schlautmann (microfabrication) and J. Martinez (image processing) for their technical support and also Prof. F. Grieser and Prof. M. Ashokkumar for fruitful discussions. The advices from Prof. C.-D. Ohl and Dr. Tandiono on the experimental pressure measurements is highly appreciated. This research was supported by the Technology Foundation STW, Applied Science Division of NWO and the Technology Programme of the Ministry of Economic Affairs, The Netherlands.

#### References

- [1] M. Ashokkumar, T.J. Mason, *Sonochemistry*, John Wiley & Sons, Inc., 2000.
- [2] A. Gedanken, *Sonochemistry and its application to nanochemistry*, *Curr. Sci.* 85 (12) (2003) 1730–1734.
- [3] N. Mahamuni, Y. Adewuyi, *Advanced oxidation processes (AOPs) involving ultrasound for waste water treatment: A review with emphasis on cost estimation*, *Ultrason. Sonochem.* 17 (6) (2010) 990–1003.
- [4] M. Ashokkumar, D. Sunartio, S. Kentish, R. Mawson, L. Simons, K. Vilku, C. Versteeg, *Modification of food ingredients by ultrasound to improve functionality: a preliminary study on a model system*, *Innov. Food Sci. Emerg. Technol.* 9 (2) (2008) 155–160.
- [5] D. Lohse, *Sonoluminescence-Cavitation hots up*, *Nature* 434 (2005) 33–34.
- [6] Y.T. Didenko, K.S. Suslick, *The energy efficiency of formation of photons, radicals and ions during single-bubble cavitation*, *Nature* 418 (6896) (2002) 394–397.
- [7] U. Parlitz, R. Mettin, S. Luther, I. Akhatov, M. Voss, W. Lauterborn, *Spatio-temporal dynamics of acoustic cavitation bubble clouds*, *Phil. Trans. R. Soc. Lond. A* 357 (1751) (1999) 313.
- [8] J. Appel, P. Koch, R. Mettin, D. Krefting, W. Lauterborn, *Stereoscopic high-speed recording of bubble filaments*, *Ultrason. Sonochem.* 11 (1) (2004) 39–42.
- [9] M.P. Brenner, S. Hilgenfeldt, D. Lohse, *Single-bubble sonoluminescence*, *Rev. Mod. Phys.* 74 (2002) 425–484.
- [10] K.S. Suslick, D.J. Flannigan, *Inside a collapsing bubble: sonoluminescence and the conditions during cavitation*, *Annu. Rev. Phys. Chem.* 59 (2008) 659–683.
- [11] K. Suslick, N. Eddingsaas, D. Flannigan, S. Hopkins, H. Xu, *Extreme Conditions during multibubble cavitation: sonoluminescence as a spectroscopic probe*, *Ultrason. Sonochem.* 18 (2011) 842–846.
- [12] R. Pflieger, H. Brau, S. Nikitenko, *Sonoluminescence from OH (C2 $\Sigma^+$ ) and OH (A2 $\Sigma^+$ ) radicals in Water: Evidence for Plasma Formation during multibubble cavitation*, *Chem. Eur. J.* 16 (39) (2010) 11801–11803.
- [13] F. Burdini, N. Tsochatzidis, P. Guiraud, A. Wilhelm, H. Delmas, *Characterisation of the acoustic cavitation cloud by two laser techniques*, *Ultrason. Sonochem.* 6 (1–2) (1999) 43–51.
- [14] S. Luther, R. Mettin, P. Koch, W. Lauterborn, *Observation of acoustic cavitation bubbles at 2250 frames per second*, *Ultrason. Sonochem.* 8 (3) (2001) 159–162.
- [15] N. Tsochatzidis, P. Guiraud, A. Wilhelm, H. Delmas, *Determination of velocity, size and concentration of ultrasonic cavitation bubbles by the phase-Doppler technique*, *Chem. Eng. Sci.* 56 (5) (2001) 1831–1840.
- [16] S. Labouret, J. Frohly, *Bubble size distribution estimation via void rate dissipation in gas saturated liquid. Application to ultrasonic cavitation bubble fields*, *Eur. Phys. J. AP* 19 (1) (2002) 39–54.
- [17] W. Chen, T. Matula, L. Crum, *The disappearance of ultrasound contrast bubbles: observations of bubble dissolution and cavitation nucleation*, *Ultrason. Med. Biol.* 28 (6) (2002) 793–803.
- [18] D. Sunartio, M. Ashokkumar, F. Grieser, *Study of the coalescence of acoustic bubbles as a function of frequency, power, and water-soluble additives*, *J. Am. Chem. Soc.* 129 (18) (2007) 6031–6036.
- [19] A. Brothie, F. Grieser, M. Ashokkumar, *Effect of power and frequency on bubble-size distributions in acoustic cavitation*, *Phys. Rev. Lett.* 102 (8) (2009) 84302.
- [20] C.E. Brennen, *Cavitation and Bubble Dynamics*, Oxford University Press, Oxford, 1995.
- [21] T.G. Leighton, *The Acoustic Bubble*, Academic Press, London, 1994.
- [22] M. Ashokkumar, *The Characterization of Acoustic Cavitation Bubbles-An Overview*, *Ultrason. Sonochem.* (2010).
- [23] R. Tronson, M. Ashokkumar, F. Grieser, *Comparison of the effects of water-soluble solutes on multibubble sonoluminescence generated in aqueous solutions by 20 –and 515-kHz pulsed ultrasound*, *J. Phys. Chem. B* 106 (42) (2002) 11064–11068.
- [24] K. Okitsu, T. Suzuki, N. Takenaka, H. Bandow, R. Nishimura, Y. Maeda, *Acoustic multibubble cavitation in water: A new aspect of the effect of a rare gas atmosphere on bubble temperature and its relevance to sonochemistry*, *J. Phys. Chem. B* 110 (41) (2006) 20081–20084.
- [25] T. Tuziuti, K. Yasui, Y. Iida, *Spatial study on a multibubble system for sonochemistry by laser-light scattering*, *Ultrason. Sonochem.* 12 (1–2) (2005) 73–77.
- [26] S. Hatanaka, K. Yasui, T. Kozuka, T. Tuziuti, H. Mitome, *Influence of bubble clustering on multibubble sonoluminescence*, *Ultrasonics* 40 (1–8) (2002) 655–660.
- [27] M.W.A. Kuijpers, M.F. Kemmere, J.T.F. Keurentjes, *Calorimetric study of the energy efficiency for ultrasound-induced radical formation*, *Ultrasonics* 40 (1–8) (2002) 675–678.
- [28] Z. Zeravcic, D. Lohse, W. van Saarloos, *Collective oscillations in bubble clouds*, *J. Fluid Mech.* 680 (2011) 114–149.
- [29] D. Fernandez Rivas, A. Prosperetti, A.G. Zijlstra, D. Lohse, H.J.G.E. Gardeniers, *Efficient sonochemistry through microbubbles generated with micromachined surfaces*, *Angew. Chem. Int. Ed.* 49 (50) (2010) 9699–9701.
- [30] N. Bremond, M. Arora, C.D. Ohl, D. Lohse, *Controlled multi-bubble surface cavitation*, *Phys. Rev. Lett.* 96 (2006) 224501.
- [31] N. Bremond, M. Arora, S.M. Dammer, D. Lohse, *Interaction of cavitation bubbles on a wall*, *Phys. Fluids* 18 (12) (2006).
- [32] P. Marmottant, J.P. Raven, H. Gardeniers, J.G. Bomer, S. Hilgenfeldt, *Microfluidics with ultrasound-driven bubbles*, *J. Fluid Mech.* 568 (2006) 109–118.

- [33] B.M. Borkent, S. Gekle, A. Prosperetti, D. Lohse, Nucleation threshold and deactivation mechanisms of nanoscopic cavitation nuclei, *Phys. Fluids* 21 (10) (2009).
- [34] A. van der Bos, A. Zijlstra, E. Gelderblom, M. Versluis, ilif: illumination by laser-induced fluorescence for single flash imaging on a nanoseconds timescale, *Exp. Fluids* 51 (2011) 1283–1289.
- [35] F. Meyer, Topographic distance and watershed lines, *Signal Process.* 38 (1994) 113–125.
- [36] T.J. Mason, J.P. Lorimer, D.M. Bates, Y. Zhao, Dosimetry in sonochemistry – the use of aqueous terephthalate ion as a fluorescence monitor, *Ultrason. Sonochem.* 1 (2) (1994) S91–S95.
- [37] Y. Iida, K. Yasui, T. Tuziuti, M. Sivakumar, Sonochemistry and its dosimetry, *Microchem. J.* 80 (2) (2005) 159–164.
- [38] A. Prosperetti, A. Lezzi, Bubble dynamics in a compressible liquid. Part 1. First-order theory, *J. Fluid Mech.* 168 (1986) 457–478.
- [39] R. Toegel, S. Hilgenfeldt, D. Lohse, Suppressing dissociation in sonoluminescing bubbles: the effect of excluded volume, *Phys. Rev. Lett.* 88 (2002) 034301.
- [40] R. Toegel, D. Lohse, Phase diagrams for sonoluminescing bubbles: A comparison between experiment and theory, *J. Chem. Phys.* 118 (2003) 1863.
- [41] L. Stricker, A. Prosperetti, D. Lohse, Validation of an approximate model for the thermal behavior in acoustically driven bubbles, *J. Acoust. Soc. Am.* 130 (5) (2011) 3243–3251.
- [42] T.G. Leighton, Bubble population phenomena in acoustic cavitation, *Ultrason. Sonochem.* 2 (2) (1995) S123–S136.
- [43] E.A. Neppiras, Acoustic cavitation, *Phys. Rep.* 61 (3) (1980) 159–251.
- [44] A. Zijlstra, Acoustic Surface Cavitation, Ph.D. Thesis, University of Twente, 2011.
- [45] H. Gelderblom, A. Zijlstra, L. van Wijngaarden, A. Prosperetti, Oscillations of a gas pocket on a liquid-covered solid surface, *Phys. Fluids*, ArXiv:1206.6996v1, submitted for publication.
- [46] A. Moussatov, C. Granger, B. Dubus, Cone-like bubble formation in ultrasonic cavitation field, *Ultrason. Sonochem.* 10 (4–5) (2003) 191–195.
- [47] A. Moussatov, R. Mettin, C. Granger, T. Tervo, B. Dubus, W. Lauterborn, Evolution of acoustic cavitation structures near larger emitting surface, in: *Proc. 5th World Congress on Ultrasonics*, Paris, France, 2003, pp. 955–958.
- [48] R. Mettin, S. Luther, C. Ohl, W. Lauterborn, Acoustic cavitation structures and simulations by a particle model, *Ultrason. Sonochem.* 6 (1–2) (1999) 25–29.
- [49] R. Pecha, B. Gompf, Microimplosions: cavitation collapse and shock wave emission on a nanosecond time scale, *Phys. Rev. Lett.* 84 (2000) 1328–1330.
- [50] M.P. Brenner, S. Hilgenfeldt, D. Lohse, Single bubble sonoluminescence, *Rev. Mod. Phys.* 74 (2002) 425–484.
- [51] N. Bremond, M. Arora, S.M. Dammer, D. Lohse, Interaction of cavitation bubbles on a wall, *Phys. Fluids* 18 (12) (2006) 121505.
- [52] S. Uzel, M.A. Chappell, S.J. Payne, Modeling the cycles of growth and detachment of bubbles in carbonated beverages, *J. Phys. Chem. B* 110 (14) (2006) 7579–7586.
- [53] J.B. Fowlkes, L.A. Crum, Cavitation threshold measurements for microsecond length pulses of ultrasound, *J. Acoust. Soc. Am.* 83 (6) (1988) 2190–2201.
- [54] L. Crum, Nucleation and stabilization of microbubbles in liquids, *Appl. Sci. Res.* 38 (1) (1982) 101–115.
- [55] J. Berlan, T.J. Mason, Sonochemistry: from research laboratories to industrial plants, *Ultrasonics* 30 (4) (1992) 203–212.
- [56] S. Hatanaka, H. Mitome, K. Yasui, S. Hayashi, Multibubble sonoluminescence enhancement by fluid flow, *Ultrasonics* 44 (2006) e435–e438.